

Gyrokinetic simulations of electrostatic microturbulence in ADITYA-U tokamak with argon impurity

Tajinder Singh^{1,*} , Kajal Shah² , Deepti Sharma³, Joydeep Ghosh^{3,4} , Kumarpalsinh A. Jadeja³ , Rakesh L. Tanna³ , M.B. Chowdhuri³ , Zhihong Lin⁵ , Abhijit Sen^{3,4} , Sarveshwar Sharma^{3,4}  and Animesh Kuley^{1,*} 

¹ Department of Physics, Indian Institute of Science, Bangalore 560012, India

² Pandit Deendayal Energy University, Knowledge Corridor, Raisan, Gandhinagar 382007, India

³ Institute for Plasma Research, Bhat, Gandhinagar 382428, India

⁴ Homi Bhabha National Institute, Anushaktinagar, Mumbai, Maharashtra 400094, India

⁵ Department of Physics and Astronomy, University of California Irvine, Irvine, CA 92697, United States of America

E-mail: stajinder@iisc.ac.in and akuley@iisc.ac.in

Received 16 February 2024, revised 3 June 2024

Accepted for publication 20 June 2024

Published 27 June 2024



CrossMark

Abstract

The effect of impurity on the electrostatic microturbulence in ADITYA-U tokamak is assessed using global gyrokinetic simulations. The realistic geometry and experimental profiles of the ADITYA-U are used, before and after argon gas seeding, to perform the simulations. Before the impurity seeding, the simulations show the existence of the trapped electron mode (TEM) instability in three distinct regions on the radial-poloidal plane. The mode is identified by its linear eigenmode structure and its characteristic propagation in the electron diamagnetic direction. The simulations with Ar¹⁺ impurity ions in the outer-core region show a significant reduction in the turbulence and transport due to a reduction in the linear instability drive, with respect to the case without impurity. A decrease in particle and heat transport in the outer-core region modifies the plasma density profile measured after the impurity seeding. It, thus, results in the stabilization of the TEM instability in the core region. Due to the reduced turbulence activity, the electron and ion temperatures in the central region increase by about 10%.

Keywords: tokamak, simulations, gyrokinetic, microturbulence, impurity seeding


(Some figures may appear in colour only in the online journal)

1. Introduction

The tokamak configuration has proven to be the most successful of the various magnetic confinement devices employed in the study of controlled nuclear fusion and has inspired the

construction of the largest experimental fusion reactor ITER (International Thermonuclear Experimental Reactor) [1]. This device which is presently under construction in Saint-Paul-lès-Durance, France, aims to demonstrate the viability of nuclear fusion as a long-term source of clean and unlimited energy. The key milestone in a tokamak is to confine the shaped plasma at a high temperature for sufficiently long to achieve a net fusion energy gain. Apart from its design complexities various processes make it hard to achieve. These processes include plasma instabilities, heat load at the plasma-facing components, edge localized modes (ELMs), disruptions, etc [2, 3]. Among these, the anomalous transport due

* Authors to whom any correspondence should be addressed.

 Original Content from this work may be used under the terms of the [Creative Commons Attribution 4.0 licence](https://creativecommons.org/licenses/by/4.0/). Any further distribution of this work must maintain attribution to the author(s) and the title of the work, journal citation and DOI.

to small-scale instabilities called micro-instabilities is found to be one of the major causes of the loss of particle and heat fluxes from the plasma core [4]. Decades of experimental, theoretical, and computational work have helped to improve our understanding of such microturbulence-induced transport. Various schemes are being devised and tested to control the electrostatic microturbulence arising from ion temperature gradient (ITG) and trapped electron mode (TEM) and concomitantly reducing the induced anomalous transport. For example, the impurity seeding experiments in axisymmetric tokamaks [5, 6] and non-axisymmetric stellarators [7, 8] have shown encouraging results in reducing turbulent transport.

In general, impurities are unavoidable in fusion reactors and can affect the device's performance in several ways. In simple terms, the presence of impurity ions leads to the dilution of the fusion fuel and reduces the number of useful fusion reactions. In addition, an excess amount of impurities can lead to the degradation of the plasma confinement due to the radiative collapse [9, 10]. However, a controlled injection of impurities in specific regions can be advantageous. For example, the gas puffing in the edge of tokamak enables the reduction in heat loads on the diverter or limiter plates [11] and also allows the mitigation of disruptions [12]. Importantly, impurity seeding can improve plasma confinement by reducing turbulent fluctuations and transport. In such scenarios, the impurity seeding can reduce the turbulent fluctuations due to the excitation of the radiative improved mode [13] or an enhanced $\vec{E} \times \vec{B}$ shear [5]. For example, neon gas injection experiments in DIII-D have shown reduced ITG-driven turbulent fluctuations due to an increased $\vec{E} \times \vec{B}$ shear [5]. Recently, boron powder injection experiments in LHD have shown a substantial increase in the plasma confinement, stored energy, and electron and ion temperatures, with the simultaneous reduction in the turbulent fluctuations [8]. Very recently, impurity seeding studies in H-mode plasma discharges of EAST tokamak have shown a significant increase in the ion temperature due to the increased toroidal rotation, which increases the $\vec{E} \times \vec{B}$ shear, and hence reduces the turbulence [6]. Similarly, the impurity-induced increase in the plasma temperature has been observed in several other magnetic fusion reactors such as JET [14], JT-60U [15], HL-2A [16], W7-X [7], ASDEX-U [17, 18], WEST [19], Alcator-C Mod [20]. In ADITYA-U tokamak, the impurity seeding experiments have also gained considerable attention, showing an increased central plasma temperature with a reduction in the outer-core or edge fluctuations [21]. In addition to such experiments, ADITYA-U has also made a significant contribution towards understanding the transport due to the runaway electrons [22, 23], plasma detachment [23], plasma disruptions [22, 23], cold pulse propagation [23–25], etc which are essential for the major long-term goals of the future fusion reactors such as ITER.

The numerical simulations have been performed in ADITYA-U using the fluid-based model to study the impurity transport in the presence of plasma turbulence [26–28]. However, the turbulent fluctuations in fusion plasma cover a broad range of spatial scales which includes the scales

smaller than the ion gyro radius [4]. Furthermore, it is crucial to include the resonant interaction of waves and particles, and the finite orbit effects in the model [29, 30]. Therefore, a detailed understanding of the underlying mechanisms behind the impurity-induced turbulence reduction requires a microscopic-level dynamical study of the plasma in realistic experimental scenarios. To this end, high-fidelity gyrokinetic simulations of magnetic fusion devices have proven to be an invaluable tool in studying transport induced by low frequency microturbulence [31]. For example, recently, the gyrokinetic toroidal code (GTC) has been used to validate the boron powder injection experiment in LHD [32] where the improved plasma confinement is observed [8]. Here, GTC is a Lagrangian approach-based particle-in-cell (PIC) code developed to study the transport due to microturbulence [33], Alfvén eigenmodes [34], radio frequency waves [35], and the energetic particles [36]. Recently, GTC has been used to perform the first global gyrokinetic simulations of the electrostatic microturbulence in ADITYA-U [37].

In this paper, we extend the earlier global gyrokinetic simulations to study the effect of impurities on the electrostatic microturbulence in ADITYA-U tokamak to understand the experimental results obtained using argon injection. The discharge #34528 is analyzed using GTC. During the plasma discharge, the argon gas is seeded from the outer-core region, due to which the fluctuations in that region are reduced, which leads to the increase in the central electron and ion temperatures and plasma density by $\sim 10\%$. ADITYA-U's realistic geometry and plasma profiles are used for the gyrokinetic analysis before and after argon gas seeding. The linear phase of the simulations shows the turbulence activity in three distinct regions on the radial-poloidal plane: innermost, intermediate, and near the edge or outer-core regions. The instability is identified as the TEM based on the linear eigenmode structure localized on the outer midplane side where the curvature is unfavorable and its propagation in the electron diamagnetic direction. Both before and after argon seeding, TEM in the inner regions represents the reactive instability based on $|\omega/\gamma| < 1$, however, in the outer regions $|\omega/\gamma| > 1$. Nonlinear simulations show the turbulence spreading away from the location of the linear eigenmode structure, thus, showing the radially global nature of the turbulence. In addition, the self-generated zonal flow is found to play a crucial role in regulating the transport due to TEM. Linear eigenmode corresponding to the TEM instability near the edge is thinner than that of the rest of the regions, whose linear growth rate and the nonlinear transport are considerably reduced after taking into account Ar^{1+} as the impurity ions in the gyrokinetic simulations, in addition to the thermal ions and electrons, representing the bulk plasma. This is reflected in the plasma profile at a later instant after the gas seeding, which increases the plasma density. In addition, the plasma density profile flattens in the core region due to the increased confinement. This leads to the stabilization of TEM in the innermost region due to the vanishing of the density gradient acting as a primary drive for TEM. Furthermore, the scan of the concentration of Ar^{1+} ions in the outermost region shows that the TEM growth rate and

nonlinear transport decrease almost linearly with the increase in the Ar^{1+} concentration. The simulations suggest that the impurity-induced reduced radial flux of heat and particles in the outer-core region followed by the stabilization of TEM in the innermost region due to the flattening of the electron density profile leads to an increase in plasma temperature by $\sim 10\%$.

The remainder of the paper is organized as follows: in section 2 the argon gas seeding experiment in ADITYA-U tokamak is described. Section 3 describes the model equations implemented in GTC, section 4 discusses the microturbulence simulations, and the conclusions are made in section 5.

2. Gas seeding experiment in ADITYA-U

This section briefly describes the argon seeding experiment performed in ADITYA-U tokamak [21]. ADITYA-U is a medium-sized, air-core tokamak with an ohmic plasma obtained in a circular limiter configuration with minor and major radii of 0.25 m and 0.75 m, respectively. The plasma discharges correspond to the proton and electron plasma with an effective charge of $Z_{\text{eff}} = 2.5$. Such discharges exhibit the plasma current of $\sim 100\text{--}250$ kA and duration of $\sim 100\text{--}350$ ms. During the current flat-top phase of the plasma current in the discharge #34528, the argon gas is seeded (injected) from the bottom port, located in the low field side of the tokamak. The chord average electron density in the center is $\sim 2 \times 10^{19} \text{ m}^{-3}$. The electron temperature is ~ 450 eV and 500 eV, before and after argon gas seeding, respectively. The on-axis ion temperature is assumed to be one-third of the electron temperature [37], and near the edge, electron and ion temperatures are considered the same. The form of the ion temperature profile is assumed to be the same as that of the electron temperature profile. The plasma profile and turbulent fluctuations are measured using various diagnostics before and after gas injection. The typical time difference between these two sets of measurements is ~ 20 ms, and the time duration of the argon gas pulse is ~ 2 ms. The edge plasma region is thoroughly diagnosed with several Langmuir probes. Experiments show an increased plasma confinement due to reduced fluctuations after argon seeding. More details about the experiment and measurements can be found in [21]. Figure 1 shows the plasma profile before (dashed lines) and after (solid lines) argon seeding. The plasma temperature and total density increase by about 10% due to improved plasma confinement after argon seeding. Figure 2 shows the normalized plasma profile gradient and the safety factor profile (scaled with the y-axis on the right). In the figure, $1/L_X = -\frac{\partial \ln X}{\partial r}$ is the inverse gradient scale length, where r is the local minor radius.

3. Model equations

This section describes the equations modeled in GTC [38] for the global gyrokinetic simulations of microturbulence with impurities in the electrostatic and collisionless limit. GTC makes use of a field-aligned mesh to represent the quantities

such as density and potential, being one of the prominent features of GTC. It is advantageous for the computational and numerical efficiency of the simulations without constraining the geometry. In addition, due to the anisotropic nature of microturbulence, $k_{\parallel} \ll k_{\perp}$, in the directions parallel and perpendicular to the magnetic field, it requires fewer grid points in the parallel direction than the grid points in the radial and poloidal directions, further reducing the computational cost of the simulations. The dynamics of thermal and impurity ions in the inhomogeneous magnetic field is described by the following gyrokinetic Vlasov equation

$$\left(\partial_t + \dot{\vec{X}} \cdot \nabla + v_{\parallel} \partial_{v_{\parallel}} \right) f_{\alpha} \left(\vec{X}, \mu, v_{\parallel}, t \right) = 0, \quad (1)$$

where

$$\dot{\vec{X}} = v_{\parallel} \hat{b} + \vec{v}_E + \vec{v}_d, \quad (2)$$

and

$$\dot{v}_{\parallel} = -\frac{1}{m_{\alpha}} \frac{\vec{B}^*}{B} \cdot (\mu_{\alpha} \nabla B + Z_{\alpha} \nabla \phi), \quad (3)$$

where $f_{\alpha} = f_{\alpha}(\vec{X}, \mu, v_{\parallel}, t)$ is the particle distribution function, \vec{X} represents the guiding center position of the particle, μ_{α} is the magnetic moment, v_{\parallel} is the particle velocity parallel to the magnetic field. The thermal and impurity ions are denoted by $\alpha = i, z$, respectively, \vec{v}_E is the $\vec{E} \times \vec{B}$ drift, \vec{v}_d comprises the drifts due to curvature and gradient in magnetic field. Z_{α} , m_{α} are the charge and mass of the particle, Ω_{α} is the gyro-frequency of the particle. $\vec{B}^* = \vec{B} + B v_{\parallel} / \Omega_{\alpha} (\nabla \times \hat{b})$ is the equilibrium magnetic field at the guiding center position of the particle, B is the equilibrium magnetic field at the particle position, $\hat{b} = \vec{B}/B$ is the unit vector along the magnetic field. ϕ is the electrostatic potential comprising the perturbed electrostatic non-zonal potential $\delta\phi$, and the electrostatic potential due to zonal flow ϕ_{ZF} , i.e. $\phi = \delta\phi + \phi_{ZF}$.

To reduce the noise due to Monte Carlo sampling of marker particles, a low noise δf method [39] is used in GTC. In this method, the distribution function is written as the sum of an equilibrium part and a fluctuating part, $f_{\alpha} = f_{0\alpha} + \delta f_{\alpha}$. The equilibrium part of the particle distribution satisfies the Vlasov equation, and the fluctuating part evolves with time. Further, the particle weight $w_{\alpha} = \delta f_{\alpha} / f_{\alpha}$ is introduced as an additional dynamical variable. The following equation represents the weight corresponding to the ion species

$$\frac{dw_{\alpha}}{dt} = (1 - w_{\alpha}) \left[-\vec{v}_E \cdot \frac{\nabla f_{0\alpha}}{f_{0\alpha}} + \frac{Z_{\alpha} \vec{B}^*}{m_{\alpha} B} \cdot \nabla \phi \frac{1}{f_{0\alpha}} \frac{\partial f_{0\alpha}}{\partial v_{\parallel}} \right]. \quad (4)$$

A kinetic treatment of the electrons is crucial to precisely describe the electrons in the gyrokinetic framework. However, the electron parallel Courant condition [40] and high frequency oscillations due to ω_H mode [41] impose difficulties on the drift-kinetic treatment of electrons. To circumvent these obstructions, a fluid-kinetic hybrid model [42] has been implemented in GTC which has been used earlier

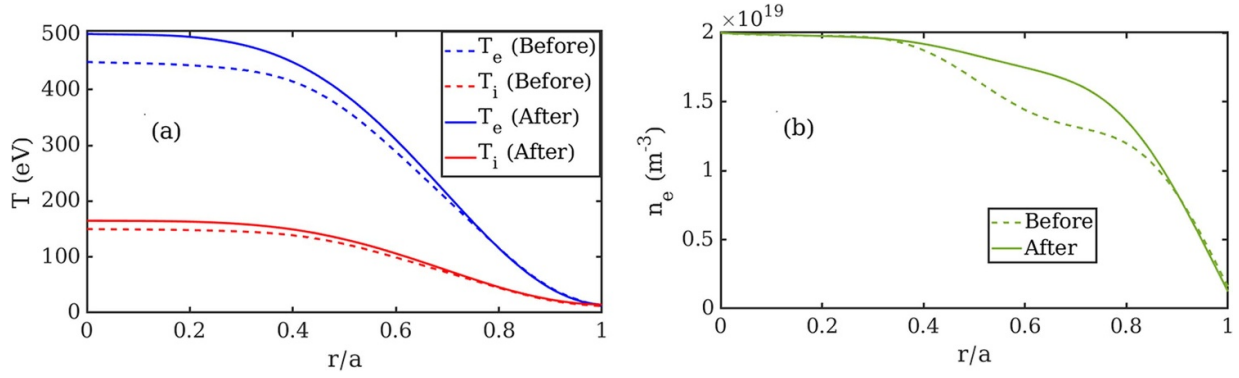


Figure 1. The plasma profile for ADITYA-U discharge #34528, before (dashed lines) and after (solid lines) argon gas seeding: (a) The electron (blue) and ion (red) temperature profiles, and (b) the electron density profile. After gas seeding the plasma profiles change, with $\sim 10\%$ increase in the central ion and electron temperatures, and the total plasma density.

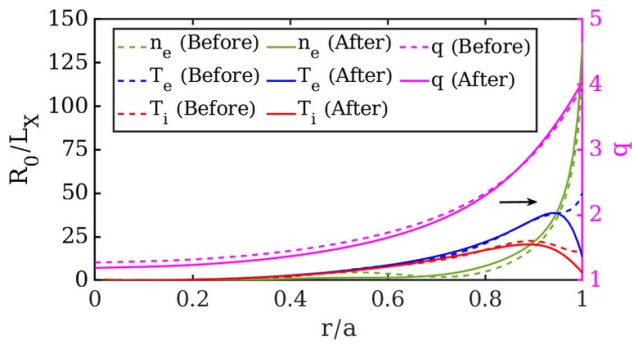


Figure 2. The radial variation of the gradient in plasma profile in the normalized units before (dashed lines) and after (solid lines) gas seeding. The safety factor profile q is presented by magenta lines scaled with the y -axis on the right.

to simulate the micro-instabilities in LHD [32, 43], W7-X [44] stellarators, and tokamak [37]. In this model, the electron distribution function is written as a sum of adiabatic and non-adiabatic parts, $f_e = f_0 e^{e\phi/T_e} + \delta g_e$. To the lowest order, the electron response is adiabatic and non-adiabatic parts represent the higher order response. The electron weight $w_e = \delta g_e / f_\alpha$ satisfies

$$\frac{dw_e}{dt} = \left(1 - \frac{e\delta\phi^{(0)}}{T_e} - w_e \right) \left[-\vec{v}_E \cdot \nabla \ln f_{e0} |_{v_\perp} - \frac{\partial}{\partial t} \left(\frac{e\delta\phi^{(0)}}{T_e} \right) - (\vec{v}_d + \delta\vec{v}_E) \cdot \nabla \left(\frac{e\phi}{T_e} \right) \right], \quad (5)$$

where $\delta\vec{v}_E = (c/B^*)\hat{b} \times \nabla \delta\phi$, and v_\perp is held fixed while writing the gradient operator on $\ln f_{e0}$ inside the square brackets on the right-hand side. Some approximations are used while writing equation (5). For example, the exact perturbed potential $\delta\phi$ on the right-hand side is approximated by the lowest order solution $\delta\phi^{(0)}$, the equilibrium pressure gradient scale length is assumed to be much longer than the perturbation scale length, and the wavelength of the electrostatic fluctuations is also assumed to be much longer than the electron gyro-radius. Following gyrokinetic Poisson equation gives the electrostatic potential

$$\sum_{\alpha=i,z} \frac{Z_\alpha^2 n_{0\alpha}}{T_\alpha} (\phi - \tilde{\phi}_\alpha) + \frac{e^2 n_{0e}}{T_e} \phi = (Z_i \delta \bar{n}_i + Z_z \delta \bar{n}_z - e \delta n_{e,\text{kinetic}}), \quad (6)$$

where the first term on the left-hand side is the ion polarization density [41] due to each of the ion species, n_{0e} is the equilibrium electron density, $\delta n_{e,\text{kinetic}}$ is the non-adiabatic part of the electron density at the guiding center, $\tilde{\phi}_\alpha$ is the second gyro-averaged electrostatic potential. The detailed procedure to solve the gyrokinetic Poisson equation can be found in earlier work using GTC (see [43]).

In the following section, as a first step, only the electrostatic gyrokinetic simulations of microturbulence are presented in ADITYA-U using GTC. Electromagnetic effects can affect the turbulent transport. For example, it is shown by gyrokinetic simulations that the electromagnetic effects can lead to the stabilization of ITG turbulence and, at high β values, can also cause a transition from ITG mode to kinetic ballooning mode (KBM) [45]. However, the electromagnetic effects may not be crucial for TEM [46–48]. Furthermore, the collisions between the plasma species are not considered in this work. However, the collisions between the plasma species can substantially affect the turbulence and transport. Collisions in plasma can affect turbulence and transport by changing the linear instability drive or affect the coherent phase space structures. In tokamaks, it has been investigated that the collisional effects can decrease the growth rate of ITG mode, lead to the stabilization of TEM turbulence, or cause a transition from TEM to ITG turbulence [49–51]. Recent electrostatic gyrokinetic simulations of microturbulence in ADITYA-U have shown that the collisions can reduce the linear growth rate of the TEM instability and nonlinear transport to a certain extent [37]. Given this, it would be important in the future to perform the electromagnetic global gyrokinetic simulations of microturbulence in ADITYA-U while retaining the collisional effects.

4. Microturbulence simulations

This section presents the gradient-driven global gyrokinetic simulations of microturbulence for the discharge #34528 of

ADITYA-U tokamak with argon gas seeding described in section 2, performed using GTC. The realistic equilibrium of ADITYA-U, generated using IPREQ code [52], is used for the GTC global simulations before and after argon gas seeding. The plasma profiles described in section 2 are used to analyze the argon seeding experiment in ADITYA-U before and after the gas seeding. In the simulations, both the passing and trapped electrons are used. The time step size used in the simulations is $0.01R_0/C_s$, where $C_s = \sqrt{T_e/m_i}$ represents the ion sound speed and R_0 represents the major radius. The number of electron subcycles used in the simulations is kept at 2, and 50 marker particles are used per cell. The gyrokinetic analysis is performed in the radial domain $r \in [0.27, 1.0]a$, which translates to $\psi \in [0.1, 1.0]\psi_X$ in the flux coordinates, where a is the minor radius and ψ_X is the magnetic flux at the last closed flux surface. The region close to the magnetic axis $[0, 0.1]\psi_X$ is omitted from the simulations as the plasma profile is flat (see figure 1) and thus the profile gradients are vanishingly small there (see figure 2). Such a choice of the simulation domain is further strengthened by the following discussion in this section. The radial domain is further divided into three annulus regions, with $\psi_I \in [0.1, 0.49]\psi_X$, $\psi_{II} \in [0.49, 0.90]\psi_X$, and $\psi_{III} \in [0.9, 1.0]\psi_X$ to well-resolve the instabilities. The value of $\rho^* = \rho_s/a$ is approximately 0.01 for both cases, where $\rho_s = c\sqrt{m_i T_e}/Z_i B$. The value of C_s/R_0 is $2.74 \times 10^5 \text{ s}^{-1}$ and $2.94 \times 10^5 \text{ s}^{-1}$ before and after argon gas seeding, respectively.

The non-uniform plasma profile and steep profile gradients at the plasma boundary can excite micro-instabilities. For the analysis of these instabilities in ADITYA-U for the gas seeding experiment, the convergence test is performed to optimize the turbulence mesh used in GTC simulations. For the case before gas seeding, the simulation domains consist of 150 flux surfaces, 3000 poloidal grid points in the innermost region, 120 flux surfaces, 3000 poloidal grid points in the intermediate region, and 30 flux surfaces, 4000 poloidal grid points in the outermost region. After gas seeding, the simulation domains consist of 200 flux surfaces, 3000 poloidal grid points in the inner region, and 30 flux surfaces, 4000 poloidal grid points in the outer region. For all the cases, 32 grid points in the parallel direction are used. The number of poloidal grid points is given on the reference flux surface where the mode diagnosis is performed.

Figure 3 shows the contour plot of the electrostatic potential on the poloidal plane in the linear phase of the nonlinear simulations before (3a, 3b) and after (3c, 3d) argon seeding. In all three regions, the instability is identified as TEM, based on the linear eigenmode structure, which is dominant on the outer midplane side where the curvature is unfavorable and its propagation in the electron diamagnetic direction. In the figure, the black solid curves represent the simulation domain, which is divided into three annulus domains, which are represented by the black dashed curves. The amplitudes of the electrostatic potential are normalized with the maximum values in each of the annulus regions. In contrast to the case before argon seeding, there is no unstable instability in the innermost region $\psi_I \in [0.10, 0.49]\psi_X$. This is due to the flat electron density profile and the small temperature gradient for the

case after gas seeding. In the outermost region, a large drive (profile gradient) excites the TEM instability which is consistent with the earlier gyrokinetic simulations of microturbulence in ADITYA-U using GTC [37]. It is worth mentioning that the TEM discussed in this work is collisionless trapped electron mode (CTEM), though the previously performed gyrokinetic simulations of TEM in ADITYA-U show that the collision can reduce turbulence and associated transport to a certain extent [37]. However, the collisions can have a destabilizing effect on the dissipative trapped electron mode (DTEM) [53] as has been found in the pedestal of HL-2A [54] and EAST [55].

Thorough diagnoses are made to study the properties of the TEM instability in the individual regions for both cases. These results are described in table 1. There is no instability in the innermost region (I) after gas seeding. For both the cases before and after argon seeding, the TEM in the inner regions (I and II) satisfies $|\omega/\gamma| < 1$, which is characteristic of the reactive instability [56], however, for the outer region (III) $|\omega/\gamma| > 1$.

For the nonlinear simulations, the same numerical resolution and input parameters are used as has been used in the linear simulations. After the exponential growth of the instability during the linear phase of the simulations, the turbulence saturates in the nonlinear phase of the simulations due to the nonlinear interaction of various poloidal and toroidal modes and also due to the coupling with the self-generated zonal flow ($n = 0$, $m = 0$). In the nonlinear simulations, all the modes are kept that are present in the linear phase. In the nonlinear phase of the simulations, the electrostatic potential on the poloidal plane is shown in figure 4, where the upper and lower panels represent the cases before and after argon gas seeding. The enlarged view of the turbulence structure is shown in figures 4(b) and (d), before and after gas seeding, respectively. The electrostatic potential is normalized by T_e/e . In the nonlinear phase, the turbulence spreads away from the location of the linear eigenmode. This illustrates the global nature of the turbulence in linking the turbulence and transport with the plasma profile gradient throughout the radial domain. In the nonlinear phase, due to the nonlinear mode coupling, energy transfers from higher wave number fluctuations to the lower ones. The frequency spectrum is broad in the nonlinear phase with the fluctuations over the range $\sim [0, 100]$ kHz. Similarly, the wave number spectrum spans the range $k_\theta \sim [0, 0.1] \text{ mm}^{-1}$. These results are also similar to the earlier investigations made in ADITYA-U [37].

GTC also provides the transport coefficients of heat and particle fluxes for the plasma species. Table 2 represents these values for all the simulation cases estimated using the time-average performed in the nonlinear steady state. The different values of diffusivities and conductivities in each region are attributed to the different instability drives due to the different profile gradients, which affect the transport levels in the nonlinear saturation. It is important to note that there is no turbulence-driven transport in the innermost region for the case after gas seeding due to the stabilization of the TEM instability. However, the values of some of the transport coefficients are increased slightly in the other two regions. Therefore, the stabilization of TEM in region I comes at the

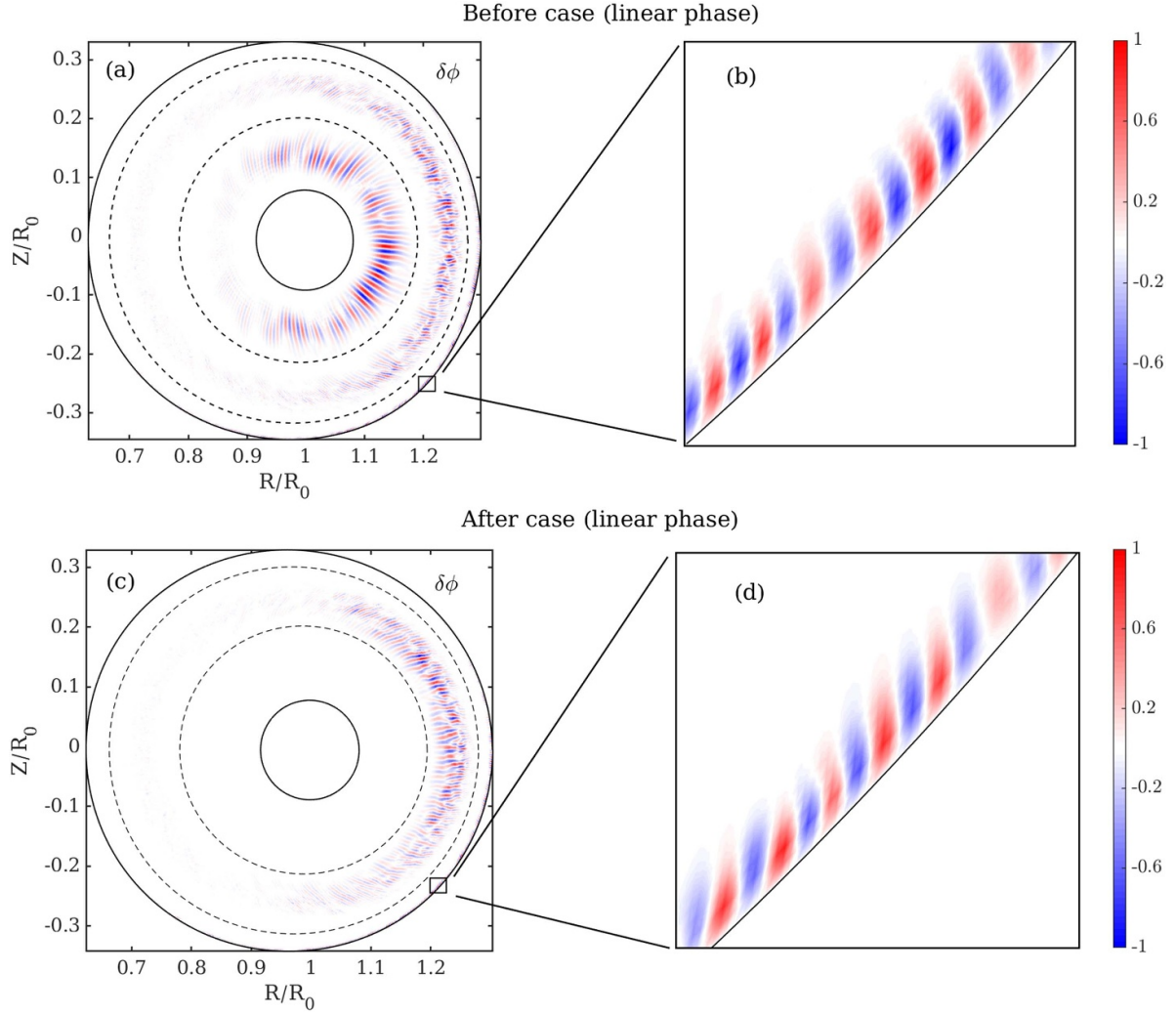


Figure 3. The contour plots of the electrostatic potential on the poloidal plane in the linear phase of the simulations before (a), (b) and after (c), (d) gas seeding. The electrostatic potential is normalized with the maximum values. In (a) and (c), the solid lines dictate the simulation boundaries which are further divided into three domains separated by the dashed lines to resolve the instabilities. The enlarged views of the linear eigenmode structures in the outer-core regions both before and after gas seeding are shown in (b) and (d), respectively. For all the cases, the dominant instability is TEM.

Table 1. Results of the linear simulations performed in the three regions for the cases before and after gas seeding. The flux surface at which the diagnosis is made is represented as ψ_d , r_d is the corresponding value in the radial domain measured on the outboard side, m and n are the dominant mode numbers in the poloidal and toroidal directions with growth rate γ and frequency ω represented in the units of C_s/R_0 , and k_θ represents the poloidal wave number. The frequency is also represented in kHz in the square brackets. The ‘dashes’ in the first row for the case after gas seeding represent the absence of instability.

Before case							
Region	ψ_d/ψ_X	r_d/a	m	n	$\gamma R_0/C_s$	$\omega R_0/C_s$ [kHz]	k_θ (mm ⁻¹)
I	0.26	0.45	69	46	1.46	1.25 [55]	0.13
II	0.76	0.83	237	96	2.12	1.50 [65]	0.14
III	~ 1	~ 1	564	145	1.72	3.95 [173]	0.17
After case							
Region	ψ_d/ψ_X	r_d/a	m	n	$\gamma R_0/C_s$	$\omega R_0/C_s$ [kHz]	k_θ (mm ⁻¹)
I	—	—	—	—	—	—	—
II	0.7	0.78	215	97	2.23	1.67 [78]	0.15
III	~ 1	~ 1	536	135	2.33	4.42 [207]	0.16

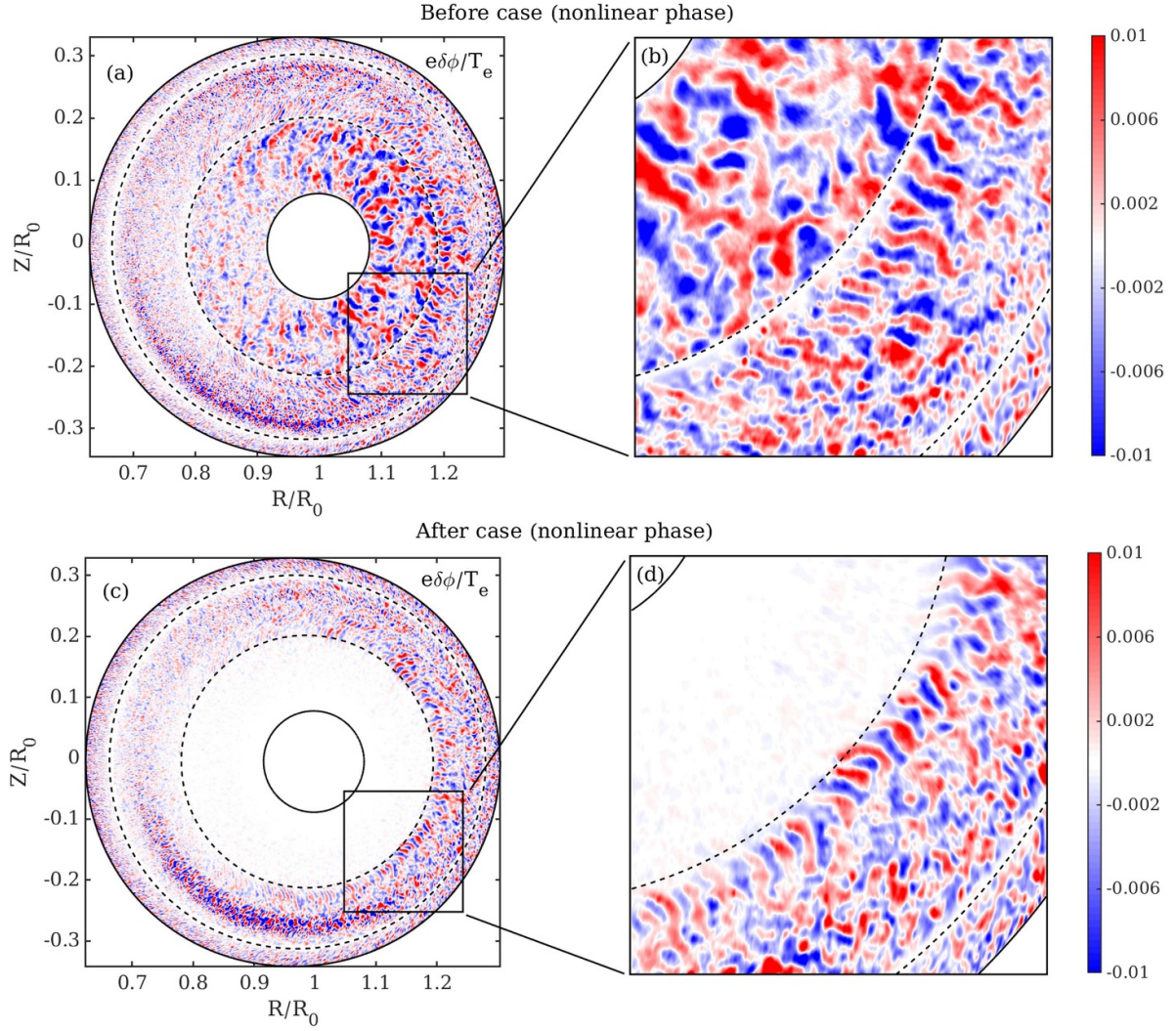


Figure 4. The contour plots of the electrostatic potential on the poloidal plane in the nonlinear phase of the simulations before (a), (b) and after (c), (d) gas seeding. The electrostatic potential is normalized by T_e/e . Following the linear phase of the simulations as shown in figure 3, in the nonlinear phase, the turbulence spread away from the region of linear eigenmode structure and thus indicates the global nature of the turbulence. The enlarged views of the turbulent eddies before and after gas seeding are shown in (b) and (d), respectively.

Table 2. The volume averaged values of the transport coefficients from the nonlinear simulations in the three regions for the cases before and after gas seeding. The heat conductivity (χ) and diffusivity (D) values for the electrons and ions are presented in $\text{m}^2 \text{s}^{-1}$. The ‘dashes’ in the first row for the case after gas seeding represents the absence of turbulence-driven transport.

Before case				
Region	χ_i	χ_e	D_i	D_e
I	1.6	1.1	0.6	0.6
II	1.6	2.1	0.5	0.5
III	1.1	1.5	0.5	0.5
After case				
Region	χ_i	χ_e	D_i	D_e
I	—	—	—	—
II	2.5	2.3	0.9	0.9
III	1.5	2.0	0.5	0.5

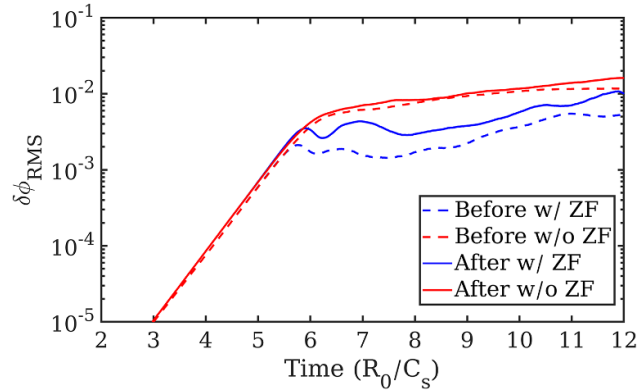


Figure 5. Time history of the root-mean-squared electrostatic potential $\delta\phi_{\text{RMS}}$ before (dashed lines) and after (solid lines) argon gas seeding, with (blue lines) and without (red lines) zonal flow, on the flux surface with $\psi = 0.69\psi_X$.

expense of increased transport in regions II and III. It is worth mentioning that in the experiments only a single argon-puff pulse is introduced (instead of a continuous train of pulses) during the discharge (see figure 2 of [21]). This single pulse changes the plasma profiles and redistributes the transport in the entire radial domain. However, to maintain the state with a modified profile, it would be necessary to introduce the argon continuously as is done in other studies [6, 8].

To study the role of zonal flow in regulating the transport due to TEM, the gyrokinetic simulations are performed by artificially suppressing the zonal flow. Figure 5 shows the time history of the root-mean-squared electrostatic potential $\delta\phi_{\text{RMS}}$ on the flux surface with $\psi = 0.69\psi_X$, for the cases before (dashed lines) and after (solid lines) argon gas seeding, with (blue lines) and without (red lines) zonal flow. The zonal flow plays a vital role in regulating the turbulent transport due to the TEM. Zonal flow suppresses the turbulent fluctuations by $\sim 70\%$ and $\sim 16\%$ for the cases before and after argon seeding. Also, it is crucial to note that the zonal flow is stronger before the gas seeding than after. The role of zonal flow in regulating the turbulent transport due to ITG and TEM turbulence has been extensively studied [57, 58]. Zonal flow affects the microturbulent transport due to the $\vec{E} \times \vec{B}$ shear which breaks the turbulent eddies into finer eddies. It is known that the zonal flow plays a crucial role in regulating the transport due to ITG turbulence [59, 60]. However, in the case of TEM turbulence, the zonal flow usually has a weaker effect. In addition, the regulation of TEM transport due to the zonal flow depends upon the parameters such as the electron to ion temperature ratio, magnetic shear, the ratio of electron temperature gradient to density gradient, and electron temperature gradient [61–66].

To understand the changes in the turbulence and transport caused by the different plasma profiles before and after argon injection, a situation is considered with the initial plasma profile, i.e. the case before argon injection, on the top of which the argon gas is introduced from the outer-core region. The gas diffuses inside the plasma and depending upon the radial variation of the bulk plasma temperature, argon gas ionizes to different charge states, which can be represented as Ar^{s+} , where s represents the ionization state of the Ar atoms, ranging

from 1 to 18. An estimate of the concentration of the individual charge states is difficult due to the occurrence of various reactions with different cross-sections. The background plasma temperature in the outer-core region is $\sim 12\text{--}15$ eV, therefore, there is a considerable accumulation of Ar^{1+} ions in this region, and the other charge states of argon have much lesser concentration. After the argon injection in the ADITYA-U tokamak, the radial profile of Ar^{1+} spectral lines are measured [21, 67]. It has been observed that the Ar^{1+} is mostly located in the edge plasma region. The total concentration of Ar^{1+} is estimated using the STRAHL code incorporating the measured Ar^{1+} spectral lines. It is important to note that the concentration of higher charge states of argon in the core is larger than that of Ar^{1+} ions in the outer-core. However, the density of the bulk plasma is much larger in the core than in the outer-core region (see figure 1(b)). Therefore, the dilution of the thermal ions by the Ar^{1+} ions in the outer-core region is more pronounced than that of the higher charge states in the core, thus, is more relevant to see a noticeable effect on the turbulence. Also, the recent simulation studies in ADITYA-U have shown the presence of Ar^{3+} ions in the outer-core region, in addition to Ar^{1+} ions [27]. Therefore, for simplicity, gyrokinetic simulations are carried out in the outer-core region by considering only the Ar^{1+} impurity ions along with the bulk plasma comprising thermal ions and electrons. The density of the impurity ions is related to bulk plasma density through the quasi-neutrality condition $Z_i n_i + Z_z n_z = n_e$, where Z_z and n_z are the charge and density of Ar^{1+} ions. Figure 6 shows the growth rate of electrostatic fluctuations near the outer-core region $\psi \sim \psi_X$ for different concentrations of Ar^{1+} . As the concentration of Ar^{1+} increases, the growth rate decreases, following almost a linear trend. Figure 7 shows the variation of the electron and ion diffusivities (D_e, D_i) and heat conductivities (χ_e, χ_i) computed near the outer-core region for different concentrations of Ar^{1+} . The transport decreases as the concentration of the Ar^{1+} increases, following almost a linear trend. It is worth mentioning that the impurities affect the ITG and TEM-driven turbulence differently. For the ITG turbulence, the effect of impurities on turbulence is mainly attributed to the change in instability drive due to the dilution of

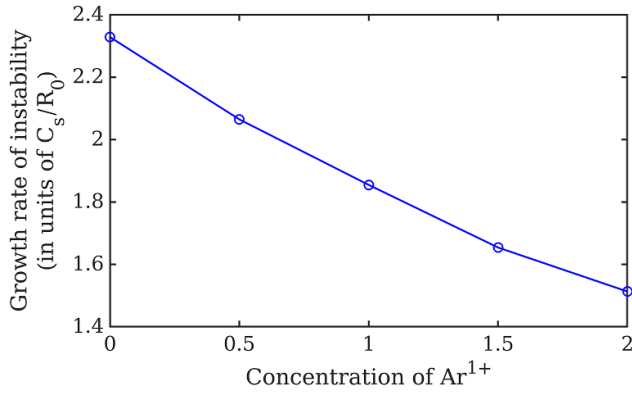


Figure 6. The variation of the linear growth rate of the instability with the concentration of Ar¹⁺ near the outer-core region. The concentration of Ar¹⁺ is presented in percentage relative to the electron density ($\frac{n_{Ar^{1+}}}{n_e} \times 100$).

main/thermal ions [68, 69] or due to the increase in $\vec{E} \times \vec{B}$ shear [5]. However, for TEM turbulence, the effect of impurities is complicated, which enters through the quasi-neutrality condition and the dispersion relation [70–72].

The reduction in the turbulent fluctuations and transport in the outer-core region accompanied by the presence of Ar¹⁺ impurity ions reduce the radial outward heat and particle fluxes. This modifies the radial density profile by increasing the electron density at a specific spatial location, i.e. an intermediate region between the edge and core. The density profile becomes more flatter in the core region, consequently the gradients in the region $r \sim [0.7, 0.9]a$ slightly increase. The flattened density profile after argon seeding has a lower density gradient. This leads to a much weaker instability drive for the TEM, and thus, the TEM gets stabilized in the innermost region for the case after argon gas seeding. Stabilization of TEM in the core results in the increased plasma temperature in the core. To strengthen the idea presented in this work, the integrated modeling of the plasma turbulence [73–75] is necessary, which requires coupling the gyrokinetic codes with the transport codes for the evolution of the plasma profile in the presence of impurity.

Furthermore, other than argon, neon is also used as an impurity in ADITYA-U experiments [76]. The gyrokinetic simulations (not described here) show a similar effect on turbulence and transport. However, from an experimental perspective, the observed differences in increasing the plasma temperature by different impurities could be due to the change in collisionality due to different masses of neon and argon. Such possibilities could be addressed in future work.

In this work, the radial electric field is not considered in the simulations, which can significantly affect the turbulence. In the earlier ADITYA-U experiments, the radial electric field is determined by toroidal rotation [77]. However, the measurements of the toroidal rotation are not available for the gas seeding experiments. Argon seeding experiments in EAST

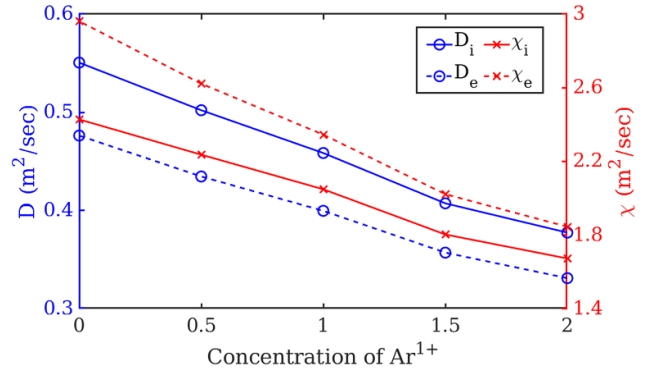


Figure 7. The variation of the ion (solid lines) and electron (dashed lines) heat conductivity (red lines scaled with the y-axis on the right) and diffusivity (blue lines scaled with the y-axis on the left) with the percentage concentration of Ar¹⁺ ions relative to the electrons near the outer-core region. The diagnosis is made at $\psi \sim \psi_X$.

tokamak [6] have shown an increased central ion temperature due to the reduction in turbulence and an increased toroidal rotation, which in turn increases the $\vec{E} \times \vec{B}$ shear. Future work could address such possibilities by developing more diagnostics in ADITYA-U tokamak.

5. Conclusions and discussion



To summarize, in this work, the effect of impurities on the electrostatic microturbulence in ADITYA-U tokamak is studied using global gyrokinetic simulations. Gyrokinetic toroidal code (GTC) is used to analyze the experimental discharge #34528 of ADITYA-U with the realistic geometry and experimental plasma profile, before and after argon gas seeding. The simulations show the turbulence activity in the three distinct regions on the radial-poloidal plane. The dominant instability is found to be TEM-driven instability depending upon the linear eigenmode structure which propagates in the direction of electron diamagnetic drift. Nonlinear simulations show the turbulence spreading away from the location of the linear eigenmode structure and illustrate the radially global nature of the turbulence. The self-generated zonal flow plays a vital role in regulating the transport due to TEM. The eigenmode structure in the outer-core region is thinner and shows a significant reduction in the linear growth rate of the fluctuations and nonlinear transport due to TEM after including the Ar¹⁺ impurity ions in the gyrokinetic simulations in addition to the thermal ions and electrons. Further, the simulations for the varying concentration of Ar¹⁺ show that the linear growth rate of the instability and nonlinear transport decreases almost linearly with the Ar¹⁺ concentration. The reduced turbulent fluctuations and transport in the outer-core region due to argon impurity seeding leads to the decrease in the radial flux of heat and particles in the outer region, which reflects in the flattening of the plasma density profile in the core in contrast to the situation before argon seeding. This leads to the stabilization of TEM in the innermost region due to the vanishingly small

density gradient, which acts as a primary drive for the TEM instability. Stabilization of TEM instability in the core leads to the increase in central ion and electron temperatures by $\sim 10\%$.

Acknowledgment

The authors thank Dr. Nirmal Bisai for his valuable input. This work is supported by the Science and Engineering Research Board EMEQ program (SERB Sanctioned No. EEQ/2022/000144), National Supercomputing Mission (NSM) (reference No. DST/NSM/R&D_HPC_Applications/Extensi-onGrant/2023/03), and Board of Research in Nuclear Sciences (BRNS Sanctioned No. 57/14/01/2022–BRNS). The computational resources of the US National Energy Research Scientific Computing Center (NERSC) and Param Pravega supercomputer at the Indian Institute of Science, Bangalore, India are used to perform the simulations presented in this work. A.S. thanks the Indian National Science Academy (INSA) for his INSA Honorary Scientist position.

ORCID iDs

Tajinder Singh  <https://orcid.org/0000-0003-0860-3626>
 Kajal Shah  <https://orcid.org/0000-0002-8056-3254>
 Joydeep Ghosh  <https://orcid.org/0000-0002-4369-1900>
 Kumarpalsinh A. Jadeja  <https://orcid.org/0000-0002-0677-0079>
 Rakesh L. Tanna  <https://orcid.org/0000-0003-4613-7072>
 M.B. Chowdhuri  <https://orcid.org/0000-0001-8313-1089>
 Zhihong Lin  <https://orcid.org/0000-0003-2007-8983>
 Abhijit Sen  <https://orcid.org/0000-0001-9878-4330>
 Sarveshwar Sharma  <https://orcid.org/0000-0002-0642-0247>
 Animesh Kuley  <https://orcid.org/0000-0003-2325-6597>

References

- [1] Green B.J. (ITER International Team and Participant Teams) 2003 *Plasma Phys. Control. Fusion* **45** 687
- [2] Wesson J. and Campbell D. 2011 *Tokamaks* (OUP Oxford)
- [3] Doyle E. et al 2007 *Nucl. Fusion* **47** S18
- [4] Horton W. 1999 *Rev. Mod. Phys.* **71** 735–78
- [5] McKee G., Burrell K., Fonck R., Jackson G., Murakami M., Staebler G., Thomas D. and West P. 2000 *Phys. Rev. Lett.* **84** 1922–5
- [6] Yang X. et al 2023 *Nucl. Fusion* **64** 016030
- [7] Lunsford R. et al 2021 *Phys. Plasmas* **28** 082506
- [8] Nespoli F. et al 2022 *Nat. Phys.* **18** 350–6
- [9] Noda N., Philipps V. and Neu R. 1997 *J. Nucl. Mater.* **241–243** 227–43
- [10] Pütterich T., Neu R., Dux R., Whiteford A., O’Mullane M. and Summers H. (the ASDEX Upgrade Team) 2010 *Nucl. Fusion* **50** 025012
- [11] Carli S., Pitts R., Bonnin X., Subba F. and Zanino R. 2018 *Nucl. Fusion* **58** 126022
- [12] Finken K., Mank G., Krämer-Flecken A. and Jaspers R. 2001 *Nucl. Fusion* **41** 1651
- [13] Boedo J., Ongena J., Sydora R., Gray D., Jachmich S., Conn R. and Messiaen A. (TEXTOR Team) 2000 *Nucl. Fusion* **40** 209
- [14] Bonanomi N., Mantica P., Citrin J., Giroud C., Lerche E., Sozzi C., Taylor D., Tsalas M. and Eester D.V. (contributors J) 2018 *Nucl. Fusion* **58** 026028
- [15] Ongena J. et al 2001 *Phys. Plasmas* **8** 2188–98
- [16] Xue G. et al 2021 *Nucl. Fusion* **61** 116048
- [17] Tardini G. et al 2012 *Plasma Phys. Control. Fusion* **55** 015010
- [18] Fable E., Kallenbach A., McDermott R., Bernert M. and Angioni C. (the ASDEX Upgrade Team) 2021 *Nucl. Fusion* **62** 024001
- [19] Yang X. et al 2020 *Nucl. Fusion* **60** 086012
- [20] Ennever P. et al 2015 *Phys. Plasmas* **22** 072507
- [21] Shah K., Ghosh J. and et al 2023 *Sci. Rep.* **13** 16087
- [22] Tanna R. et al 2019 *Nucl. Fusion* **59** 112006
- [23] Tanna R. et al 2022 *Nucl. Fusion* **62** 042017
- [24] Macwan T. et al 2021 *Nucl. Fusion* **61** 096029
- [25] Rodriguez-Fernandez P. et al 2018 *Phys. Rev. Lett.* **120** 075001
- [26] Bisai N., Chowdhuri M., Banerjee S., Raj H., Dey R., Tanna R., Manchanda R., Jadeja K. and Ghosh J. (Aditya Team) 2019 *Nucl. Fusion* **59** 126013
- [27] Raj S. et al 2022 *Nucl. Fusion* **62** 036001
- [28] Raj S., Bisai N., Shankar V. and Sen A. 2023 *Phys. Plasmas* **30** 062302
- [29] Grigory K. 2009 Finite drift orbit effects in a tokamak pedestal *PhD Thesis* Department of Physics, Massachusetts Institute of Technology USA (available at: <http://hdl.handle.net/1721.1/63005>)
- [30] Horton W. 2017 *Turbulent Transport in Magnetized Plasmas* 2nd edn (World Scientific)
- [31] Garbet X., Idomura Y., Villard L. and Watanabe T. 2010 *Nucl. Fusion* **50** 043002
- [32] Singh T., Nicolau J.H., Nespoli F., Motojima G., Lin Z., Sen A., Sharma S. and Kuley A. 2024 *Nucl. Fusion* **64** 016007
- [33] Xiao Y., Holod I., Wang Z., Lin Z. and Zhang T. 2015 *Phys. Plasmas* **22** 022516
- [34] Wang Z., Lin Z., Holod I., Heidbrink W.W., Tobias B., Van Zeeland M. and Austin M.E. 2013 *Phys. Rev. Lett.* **111** 145003
- [35] Bao J., Lin Z., Kuley A. and Lu Z. 2014 *Plasma Phys. Control. Fusion* **56** 095020
- [36] Zhang W., Lin Z. and Chen L. 2008 *Phys. Rev. Lett.* **101** 095001
- [37] Singh T., Sharma D., Macwan T., Sharma S., Ghosh J., Sen A., Lin Z. and Kuley A. 2023 *Nucl. Fusion* **63** 056008
- [38] Lin Z., Hahn T., Lee W., Tang W. and White R. 1998 *Science* **281** 1835–7
- [39] Parker S. and Lee W. 1993 *Phys. Fluids B* **5** 77–86
- [40] Sydora R., Decyk V. and Dawson J. 1996 *Plasma Phys. Control. Fusion* **38** A281
- [41] Lee W. 1987 *J. Comput. Phys.* **72** 243–69
- [42] Lin Z., Nishimura Y., Xiao Y., Holod I., Zhang W. and Chen L. 2007 *Plasma Phys. Control. Fusion* **49** B163–72
- [43] Singh T., Nicolau J.H., Lin Z., Sharma S., Sen A. and Kuley A. 2022 *Nucl. Fusion* **62** 126006
- [44] Nicolau J.H., Choi G., Fu J., Liu P., Wei X. and Lin Z. 2021 *Nucl. Fusion* **61** 126041
- [45] Ishizawa A., Imadera K., Nakamura Y. and Kishimoto Y. 2019 *Phys. Plasmas* **26** 082301
- [46] Belli E.A. and Candy J. 2010 *Phys. Plasmas* **17** 112314
- [47] Ishizawa A., Maeyama S., Watanabe T.H., Sugama H. and Nakajima N. 2015 *J. Plasma Phys.* **81** 435810203
- [48] Hu Y.C. et al 2023 *Plasma Phys. Control. Fusion* **65** 055023
- [49] Ajay C.J., Brunner S. and Ball J. 2021 *Phys. Plasmas* **28** 092303
- [50] Ryter F., Angioni C., Peeters A., Leuterer F., Fahrbach H.U. and Suttrop W. (the ASDEX Upgrade Team) 2005 *Phys. Rev. Lett.* **95** 085001
- [51] Hu W., Feng H.Y. and Dong C. 2018 *Chin. Phys. Lett.* **35** 105201

- [52] Sharma D., Srinivasan R., Ghosh J. and Chattopadhyay P. 2020 *Fusion Eng. Des.* **160** 111933
- [53] Kadomtsev B. and Pogutse O. 1971 *Nucl. Fusion* **11** 67
- [54] Wen J. *et al* 2023 *Phys. Plasmas* **30** 112502
- [55] Wang H.Q. *et al* 2014 *Phys. Rev. Lett.* **112** 185004
- [56] Fulton D., Lin Z., Holod I. and Xiao Y. 2014 *Phys. Plasmas* **21** 042110
- [57] Diamond P., Itoh S.I., Itoh K. and Hahm T. 2005 *Plasma Phys. Control. Fusion* **47** R35
- [58] Chen H. and Chen L. 2022 *Phys. Rev. Lett.* **128** 025003
- [59] Makwana K.D., Terry P.W., Pueschel M.J. and Hatch D.R. 2014 *Phys. Rev. Lett.* **112** 095002
- [60] Chen L., Lin Z. and White R. 2000 *Phys. Plasmas* **7** 3129–32
- [61] Merz F. and Jenko F. 2008 *Phys. Rev. Lett.* **100** 035005
- [62] Lang J., Chen Y. and Parker S.E. 2007 *Phys. Plasmas* **14** 082315
- [63] Lang J., Parker S.E. and Chen Y. 2008 *Phys. Plasmas* **15** 055907
- [64] Ernst D., Lang J., Nevins W., Hoffman M., Chen Y., Dorland W. and Parker S. 2009 *Phys. Plasmas* **16** 055906
- [65] Dannert T. and Jenko F. 2005 *Phys. Plasmas* **12** 072309
- [66] Xiao Y. and Lin Z. 2009 *Phys. Rev. Lett.* **103** 085004
- [67] Shah K. *et al* 2021 *Rev. Sci. Instrum.* **92** 053548
- [68] Paccagnella R., Romanelli F. and Briguglio S. 1990 *Nucl. Fusion* **30** 545
- [69] Frojdh M., Liljestrom M. and Nordman H. 1992 *Nucl. Fusion* **32** 419
- [70] Du H., Wang Z.X. and Dong J.Q. 2016 *Phys. Plasmas* **23** 072106
- [71] Zhang X.R. *et al* 2021 *Phys. Plasmas* **28** 052510
- [72] Shen Y., Dong J.Q., Sun A.P., Qu H.P., Lu G.M., He Z.X., He H.D. and Wang L.F. 2016 *Plasma Phys. Control. Fusion* **58** 045028
- [73] Rodriguez-Fernandez P. *et al* 2019 *Phys. Plasmas* **26** 062503
- [74] Angioni C., Fable E., Ryter F., Rodriguez-Fernandez P. and Pütterich T. (the ASDEX Upgrade Team) 2019 *Nucl. Fusion* **59** 106007
- [75] Citrin J. *et al* 2022 *Nucl. Fusion* **62** 086025
- [76] Chowdhuri M.B. and *et al* 2018 *Proc. 27th IAEA Fusion Energy Conf. (FEC) (Gandhinagar, India, 22–27 October 2018)* (available at: [https://nucleus.iaea.org/sites/fusionportal/Shared Documents/FEC 2018/fec2018-preprints/preprint0578.pdf](https://nucleus.iaea.org/sites/fusionportal/Shared%20Documents/FEC%2018/fec2018-preprints/preprint0578.pdf))
- [77] Shukla G. *et al* 2019 *Nucl. Fusion* **59** 106049